Contribution of Capillary Adhesion to Friction at Macroscopic Solid–Solid Interfaces

Feng-Chun Hsia[1,2] Chao-Chun Hsu,[3] Liang Peng,[2] Fiona M. Elam,[1] Chen Xiao,[1,2]
Steve Franklin[1,4] Daniel Bonn,[2] and Bart Weber[1,2,*]

[1] *Advanced Research Center for Nanolithography (ARCNL), Science Park 106, 1098 XG Amsterdam, Netherlands*

[2] *Van der Waals-Zeeman Institute, Institute of Physics, University of Amsterdam, Science Park 904, 1098 XH Amsterdam, Netherlands*

[3] *Van't Hoff Institute for Molecular Sciences, University of Amsterdam, Science Park 904, 1098 XH Amsterdam, Netherlands*

[4] *Department of Materials Science and Engineering, The University of Sheffield, Sheffield S1 3JD, United Kingdom*

Capillary adhesion is commonly present in ambient conditions. It can be measured in single-asperity contacts through atomic force microscopy using a sharp probe that is pulled off a smooth substrate. However, for macroscopic multiasperity interfaces, the measured adhesive force is always close to zero because of the elastic energy stored into the deformation of surface roughness; this is known as the adhesion paradox. Here, we experimentally show how capillary adhesion influences friction between macroscopic Si-on-Si interfaces, covered with native oxide, in two vapor environments: humid air and isopropyl alcohol (IPA) vapor. To quantify the adhesion contribution to friction, we present a boundary element method that successfully models the interplay between capillary adhesion, surface topography, and friction without adjustable parameters and show that the evolution of the surface topography during sliding dramatically increases capillary adhesion and thus friction. Replacing the water vapor with an organic (IPA) vapor, we find a lower adhesion due to the smaller surface tension.

I. INTRODUCTION

Approximately 71% of the surface of the Earth is covered by water. The polarity of water molecules induces strong cohesive and adhesive forces between water and hydrophilic surfaces, causing water to condense at free and contacting surfaces in humid environments. The presence of water at interfaces between hydrophilic surfaces is ubiquitous and leads to capillary adhesion. This is caused by capillary bridges that typically display negative curvature in the direction normal to the interface, leading to a Laplace pressure difference between the fluid inside the bridge and the surrounding gas, which in turn causes attraction of the surfaces to each other [1,2]. This capillary attraction contributes to the ability of insects to walk vertically [2–4], dictates the mechanics of granular materials [5], and leads to failure in micro- and nanoelectromechanical systems (MEMS and NEMS) [6–12]. Moreover, the car industry, 5G networks, artificial intelligence, and high-performance computing all rely on the production of modern integrated circuits which currently are scarce. Nanoscale tribological phenomena (i.e., friction and wear)

form one of the challenges in the high-precision positioning [13–16] that is required for efficient chip production.

The effect of capillary adhesion on the contact mechanics and friction behavior of nanoscale single-asperity interfaces is widely studied [17–19]. Many atomic force microscopy (AFM) experiments display a strong dependence of the capillary adhesion or friction on relative humidity (RH) [17,19,20]. Besides direct adhesion [19,21], displacement of the three-phase contact line of the capillary meniscus also leads to friction [22]. Furthermore, the structure of the absorbed water layer affects the adhesion and friction at single nanoasperity contacts [19,23–27]. However, the relative importance of mechanisms that control single-asperity adhesion and friction is not necessarily identical to that for multiasperity contacts. It is important to note that the typical asperity aspect ratios can vary at multiasperity interfaces, leading to changes in the relative importance of adhesion exerted across finite gaps at the interface [28]. For smooth multiasperity contacts, the adhesion exerted within the area of real contact can become significant compared to the normal stress exerted within these contacts. In this situation, the friction will become proportional to the area of real contact with a proportionality constant that is set by the solid-on-solid

*b.weber@arcnl.nl

034034-1

adhesion [29–32]. Furthermore, at multiasperity interfaces the presence or absence of a few tall asperities can completely change the sliding behavior [33]. Surface topography can influence the uniformity of the water condensate thickness [34] and the number of capillary bridges that can form across the interface [35,36], thereby determining the capillary adhesion exerted at the interface.

Direct measurement of adhesion between macroscopic objects is often problematic because of the adhesion paradox [37]: despite the strong adhesive interactions that many solids undergo at the nanoscale, they rarely stick at the macroscopic scale [28]. The adhesion typically is short-ranged [38], and upon unloading the interface this adhesion is cancelled by the elastic energy stored in the larger-scale elastic deformation of roughness. In addition, the topography of rubbing surfaces is constantly changed by wear [33,39]. The evolution of the surface topography and the generation of wear debris then lead to temporal variations in the capillary adhesion. The contribution of capillary adhesion to friction in macroscopic contacts therefore remains difficult to quantify, which is one of the fundamental problems for understanding the friction between macroscopic bodies. Furthermore, while there is extensive work on single-asperity contacts describing capillary adhesion and friction [17–19,21,22,26,40], few studies [2,31,41] have aimed to bridge from nanoscale adhesion measurements to the macroscale multiasperity manifestation of capillary adhesion and its influence on friction.

In this work, we show how capillary adhesion, and the contribution of capillary adhesion to friction, can be quantified through friction measurements in vapor- and liquid-immersed environments. Our experiments show that capillary adhesion significantly contributes to friction at multiasperity Si-on-Si interfaces that are covered with a native oxide. The experimental results can be reproduced by a simple capillary adhesion model, without adjustable parameters, that is based on boundary element contact calculations. When compared, the experiments and model calculations demonstrate that the capillary adhesion is very sensitive to wear; removal of the highest asperities at the interface strongly reduces the average separation, thereby increasing the adhesion by bringing the two surfaces closer together.

In addition to water measurements, we perform the same experiments when the surfaces are brought into contact with an isopropyl alcohol (IPA) vapor. In agreement with our model, the adhesion is weaker due to the lower surface tension and higher volatility. For both liquids, if the contact is fully immersed, we find that the friction is significantly lower, demonstrating directly that the capillary bridges typically contribute about 30% to the total friction in a partially saturated environment. We also find that the fully immersed IPA contact has a significantly lower friction than the fully immersed water contact and attribute this difference to IPA boundary lubrication. While our work focuses on Si-on-Si interfaces, the observed behavior is representative of interfaces between stiff and hydrophilic materials [31].

II. RESULTS AND DISCUSSION

A. Adhesion at single-asperity contacts

To relate adhesion at single-asperity interfaces to adhesion at multiasperity interfaces, we perform pull-off experiments at single and multiasperity Si-on-Si hydrophilic interfaces. The single-asperity AFM-based experiments (see Appendix A) were performed in both water-rich and IPA-rich vapor environments. Control over the environment was obtained by introducing a 0.5 l/min air flow into a semiopen fluid AFM cell (Bruker). The air flow consisted of dry nitrogen that was passed through a gas wash bottle filled with either water or IPA. This resulted in an RH of $58 \pm 0.7\%$ inside the AFM cell when the air flow was bubbled through water. The partial pressure of IPA in the AFM cell resulting from bubbling the dry nitrogen through IPA could not be measured directly and is treated as unknown.

In both water and IPA environments, a Si AFM tip was moved toward the surface of a Si wafer and retracted afterwards at a speed of 5 nm/s, sufficiently slow to warrant (near) equilibrium conditions [27,42,43]. The externally applied normal force (F) on the tip was measured through the deflection of the AFM cantilever as a function of the normal displacement (D) resulting in a typical F-D curve [Figs. 1(a) and 1(b)]. Such F-D curves clearly indicate that the tip snaps into contact roughly 4 nm [W_{tip} in Fig. 1(a)] before a repulsive force is detected on the AFM cantilever [27]. In the repulsive part of the F-D curve, the measured normal force increases linearly with displacement at a rate that is set by the stiffness of the AFM cantilever, 42 N/m in our experiments. Upon retraction of the probe, we measured an F-D curve that approximately follows the approach curve, except for the important distinction that the probe can be retracted by up to 10 nm beyond the snap-in point before the probe is completely pulled off the surface and no normal force is measured. This rather long pull-off distance is often interpreted [27] in the context of capillary adhesion; the reduced pressure inside a negatively curved capillary bridge between tip and substrate causes an attractive force [inset of Fig. 1(b)] and the attractive force is gradually reduced as the tip is separated from the substrate and the capillary bridge is stretched [36].

To test this interpretation, we also performed F-D measurements with the tip-substrate interface fully immersed in liquid water or IPA [inset of Figs. 1(a) and 1(b)]. Indeed, the adhesive strength and range are strongly reduced in liquid-immersed experiments; since there is no gas phase available, capillary bridges cannot form. We define the adhesive force as the difference between the minimum
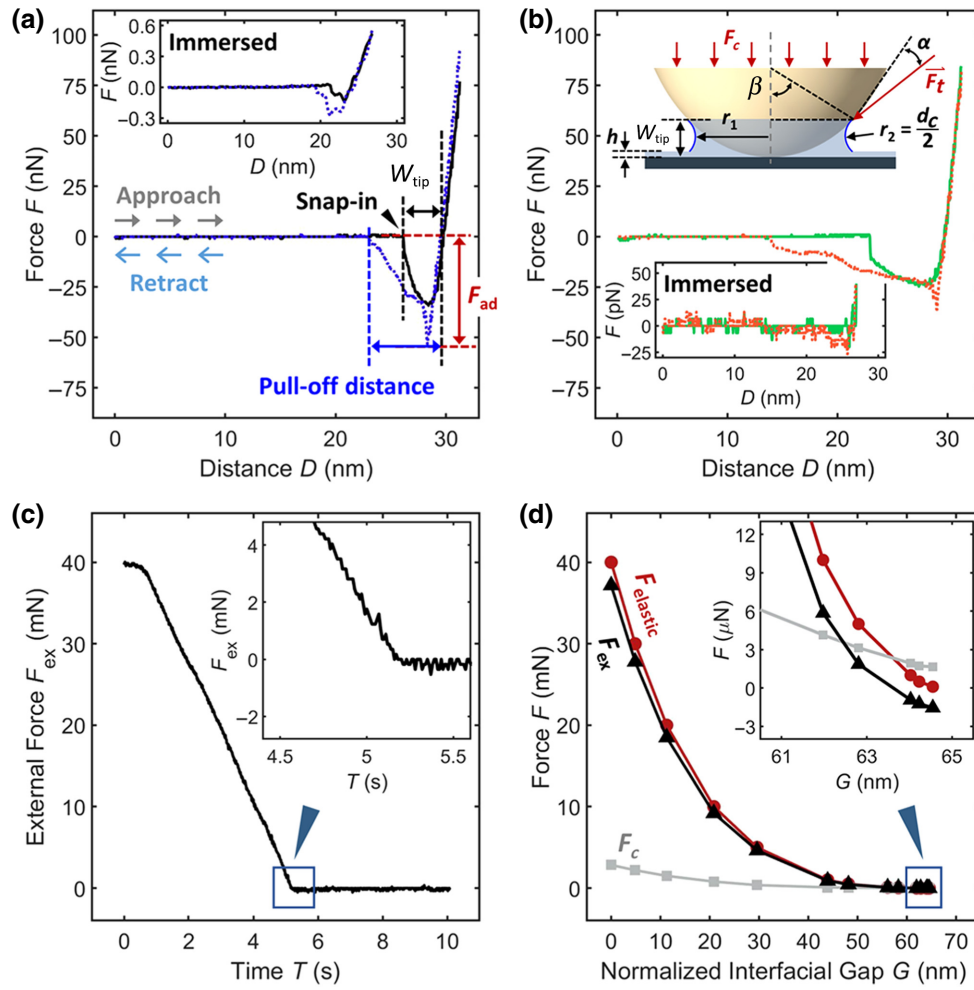
FIG. 1. Single nanoasperity and macroscopic multiasperity pull-off force measurements and calculations. (a) A typical force-displacement (F-D) curve measured at a relative humidity (RH) of 58%, showing the tip-sample normal force measured as the tip approaches the sample and as the tip is retracted. (b) An F-D curve measured in an isopropyl alcohol (IPA) rich vapor environment. The inset (a) and lower inset (b) display an F-D curve measured while the tip-sample interface is immersed in liquid water and IPA, respectively. The upper inset (b) illustrates a capillary bridge and the capillary and tension forces exerted at such a bridge. (c) External force (F_{ex}) as a function of time (T) measured during the retraction of a Si ball from a Si wafer surface; the inset shows a close-up. (d) The calculation of capillary adhesion (F_c) exerted at the Si ball-on-Si wafer interface as a function of the average interfacial gap relative to the average interfacial gap corresponding to an elastic force of 40 mN. The inset shows that as the elastic force ($F_{elastic}$) decreases to zero the capillary adhesive and external force, both of the order of μN, cancel each other. The experiments and calculations in (c) and (d) were conducted at an RH of $53 \pm 1.4\%$ and 50%, respectively.

force and the force measured when there is no interaction between the tip and the substrate [Fig. 1(a)]. To further understand the nature of the adhesion, we calculate the adhesive force using the model from Ref. [20] which incorporates three contributions: (i) the capillary force caused by the Laplace pressure acting over the area on the tip that is wetted by the capillary bridge [$F_c = \gamma(1/r_1 + 1/r_2)\pi R^2$]; (ii) the tension force [$F_t = 2\pi R\gamma \cos(\alpha)\sin(\beta)$] caused by the surface tension acting on the three-phase contact line of the capillary bridge; (iii) the van der Waals force {$F_v = [H_{air}(1 - A_{Rel}) + H_{water}A_{Rel}]R_{tip}/(6d_a^2)$} that causes attraction of the solids across an air or liquid

medium (see I in the Supplemental Material for details [44]). The adhesion model approximates the tip–sample interface as a sphere-on-flat interface and can be evaluated if the tip radius and the amount of water present at the interface are known. The former we obtain through tip deconvolution ($R_{tip} = 28 \pm 2$ nm, see II in the Supplemental Material [44]), and the latter we infer from the literature [45,46]; both the critical distance for capillary condensation [$d_c = 3$ nm; see Fig. 1(b) inset] and the thickness of condensed water on a free Si substrate [$h = 1.2$ nm; see Fig. 1(b) inset] were measured at the relative humidity corresponding to our experiment ($58 \pm 0.7\%$).

We find good agreement between the adhesion model prediction (54 ± 4 nN), without adjustable parameters, and the adhesion experiment conducted in the 58% RH environment (52 ± 15 nN). The capillary force (F_c) is responsible for approximately 80% of the total adhesive force according to the model: indeed, capillary adhesion is the dominant adhesion mechanism. Furthermore, the observed snap-in distance (W_{tip}) in the experiments [see Fig. 1(a)] was 3.9 ± 0.2 nm, close to that observed in tuning-fork-based experiments: $W_{tip} = h + d_c = 4.2 \pm 0.3$ nm at 58% RH (Table SI in the Supplemental Material [44]) [45,46]. The error quantifies the standard deviation of the distribution of pull-off forces that were observed (Fig. S2 in the Supplemental Material [44]). This variation in pull-off forces is thought to result from a thermally activated pull-off process [47]. In the measurements conducted with the same AFM tip in an IPA-rich environment, we observe a snap-in distance of $W_{tip} = 7 \pm 0.7$ nm and an adhesive force of 34 ± 14 nN. Interestingly, in comparison to the humid measurements, the adhesive force is smaller while the area of the tip that is wetted by the capillary bridge must be larger, due to the increased snap-in distance [48,49]. The capillary force (F_c), the tension force (F_t) and the van der Waals force (F_v) are likely all reduced when IPA is introduced into the environment while water is removed. Capillary force and tension force are proportional to the liquid surface tension, which is lower for IPA than for water. The van der Waals force scales with the difference in refractive index between silicon and the medium in between the tip and the substrate. Since IPA has a higher refractive index than water, this force should also decrease upon the introduction of IPA [50]. However, since the capillary force is dominant, we focus our discussion on this force.

The capillary force is the product of the tip area that is wetted by a capillary bridge and the Laplace pressure difference, $P_{\mathrm{Laplace}} = \gamma/R$, with γ the liquid surface tension and R the radius of curvature of the capillary bridge. As water at the interface is replaced with IPA, the wetted area of the tip and the curvature of the capillary bridge change slightly [45,49], while the surface tension drops by a factor of 3 ($\gamma_{\mathrm{IPA}} = 23.8$ mN/m [51] and $\gamma_{\mathrm{water}} = 72.8$ mN/m [52]). We argue that this strong reduction in surface tension thus drives the drop in adhesive force observed when the humid environment is dried and IPA is introduced at the interface. The AFM experiments show that capillary adhesion is the dominant adhesion mechanism at single-asperity Si-on-Si interfaces. Reduction of the humidity and introduction of IPA into the environment of the contact strongly reduces the capillary adhesion while increasing its range.

B. Adhesion at multiasperity contacts

Virtually all frictional interfaces are multiasperity; the key question is how the capillary adhesion that dominates single-asperity Si-on-Si interfaces manifests itself at larger multiasperity Si-on-Si interfaces. To answer this question, we performed ball-on-flat pull-off experiments. In the pull-off experiments a 3-mm-diameter Si ball was brought into contact with a Si wafer in a 53% RH air environment, after which a load of 40 mN was applied and the ball was pulled ball back up [see Fig. 1(c) and Appendix B]. Perhaps surprisingly, within the millinewton accuracy of the experiment, no pull-off force was detected [inset of Fig. 1(c)]. It should be noted that the high stiffness of the force sensor, combined with the pull-off speed, limits the sensitivity to adhesion of the macroscale adhesion experiment (see Appendix B for details). The force balance at the interface requires that the capillary adhesion (F_c) and the externally applied load (F_{ex}) cancel the elastic force (F_{elastic}) generated by the compressed asperities at the interface: $\vec{F}_{\mathrm{elastic}} = \vec{F}_{ex} + \vec{F}_c$. During pull-off, the external load vanishes. The capillary bridges pull the two surfaces together, but in doing so elastically deform the asperities, thereby generating an elastic counterforce. Due to the high stiffness of the Si asperities, the elastic energy dominates over the adhesion energy. This is the reason why no pull-off force is measured, and the origin of the adhesion paradox.

To understand what happens quantitatively, we carried out boundary element method (BEM) contact calculations (see Appendix D) to estimate the elastic and capillary force at multiasperity interfaces as a function of interfacial gap [Fig. 1(d)]. The BEM contact calculation takes the surface topography of the pristine Si ball, measured by AFM [Fig. 2(a)], as input together with the mechanical properties of Si as listed in Table SII in the Supplemental Material [44] (see Appendix C). The BEM solver subsequently calculates how the topography is elastically deformed by a given load (F_{elastic}) in the absence of adhesion. The resulting interface gap profile can be used to estimate the capillary force associated with that interface geometry. To roughly estimate the capillary force, we assume (as in the single-asperity AFM experiments) that water can condense at regions of the interface within which the interfacial gap is finite but smaller than $W = 2h + d_c$ [see Fig. 1(b) inset; we assume a water layer of equilibrium thickness on both surfaces]. Across this area within which capillary condensation can take place, a Laplace pressure difference caused by the negative curvature of the water–air interface in the direction normal to the contact leads to capillary attraction. To estimate the capillary force (F_c), we multiply the Laplace pressure difference by the area of the interface at which the gap is larger than zero and smaller than W. The equilibrium values for both W and the Laplace pressure difference can be obtained from the literature [45,49] as a function of RH. Furthermore, our single-asperity experiments (Fig. 1) with the same materials confirm the range and strength of the capillary adhesion
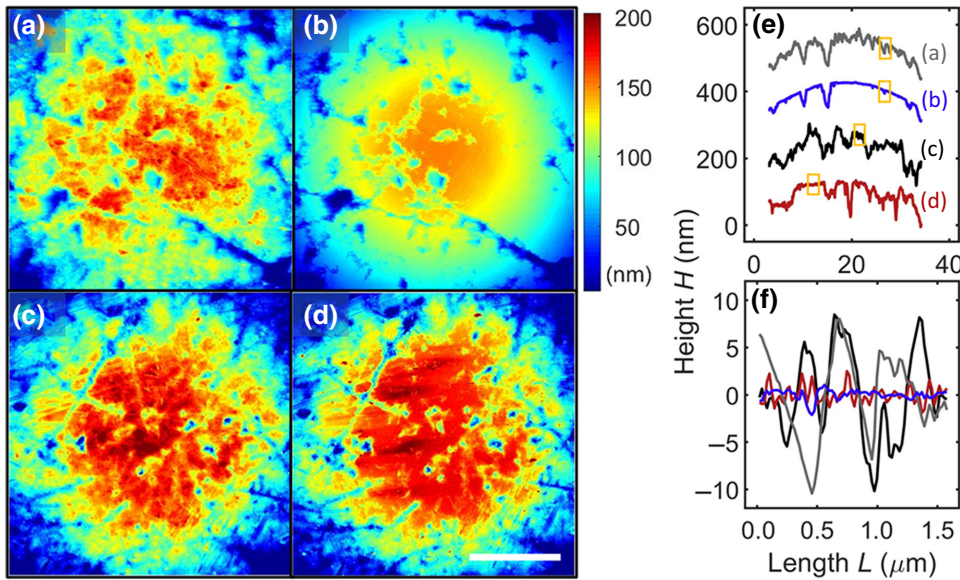
FIG. 2. Atomic force microscopy (AFM) surface topography of Si balls. The AFM topography of (a) a pristine Si ball and (b) an artificially worn Si ball. The AFM topography of a pristine Si ball (c) before sliding and (d) after 190 μm sliding at a velocity of 1 μm/s and a normal force of 40 mN. The AFM topographies are measured over a 31 μm $\times$ 31 μm scan area with 430.6 nm^2 pixel size. (e) The cross-section height profile (H) of the topographies shown in (a)–(d). (f) Zoom-in height profile corresponding to the orange boxes in (e). Scale bar 10 μm.

found in the literature. Subsequently the external force at which the calculated interface is balanced is given by $\vec{F}_{\mathrm{ex}} = \vec{F}_{\mathrm{elastic}} + \vec{F}_c$.

The result of the calculations, conducted for various elastic forces (F_{elastic}), is summarized in Fig. 1(d). The calculations show that the pull-off force (F_{ex}) is negligible (of the order of micronewtons) compared to the millinewton accuracy of the experiment; multiasperity adhesion may be significant at a loaded interface but disappears due to the elasticity of the asperities when the external load is removed. Rough estimates of the elastic and adhesion energy can be obtained by integrating the calculated force distance curve upon loading (assuming 10^5 N/m contact stiffness [31]): 20 mN $\times$ 400 nm $= 8 \times 10^{-9}$ J, and by multiplying the water surface tension with the area of apparent contact [Fig 4(c)]: $72.8 \times 10^{-3} \times [\pi(10 \times 10^{-6})^2] = 2.3 \times 10^{-11}$ J. Indeed, this estimate confirms that for this stiff system elastic energy dominates over surface energy. This destructive interplay between adhesion and elasticity is known as the adhesion paradox; despite strong adhesive interactions at the molecular scale, larger interfaces usually do not display stickiness because the elasticity of compressed asperities cancels out the adhesion when the external load is removed [41].

C. Capillary adhesion and friction

The adhesion paradox thus prevents direct measurement of Si ball-on-Si wafer multiasperity adhesion through pull-off experiments. This makes it challenging to understand how the adhesion contributes to the friction at such interfaces. To elucidate the contribution to friction of capillary adhesion, we perform Si ball-on-Si wafer sliding experiments [Fig. 3(a)] in ambient (41 $\pm$ 1% RH) and IPA vapor

as well as liquid environments (see Appendix E). The frictional force (F_f) was measured during sliding and converted into a coefficient of friction (COF), which is the ratio of frictional force to normal force (F_n): COF $= F_f / F_n$. We confirmed that the COF was well defined and independent of the normal force (Fig. S3 in the Supplemental Material [44]).

The friction experiments show that the COF measured in ambient and IPA vapor environments is significantly higher than the COF measured in water and IPA immersed environments [Fig. 3(b)]. At low sliding speeds ($V = 1$ μm/s) the high Si ball-on-Si wafer contact pressure ($P_{\mathrm{Hertz}} \approx 250$ MPa) in combination with the low viscosity of the fluids (eta water $= 1.0 \times 10^{-3}$ Pa s and eta IPA $= 2.4 \times 10^{-3}$ Pa s at 20 °C) clearly excludes hydrodynamic lubrication, and places the sliding system in the boundary lubrication regime (Hersey number 10^{-13}). We therefore argue that since both water and IPA form thick boundary layers on Si when presented in the gas phase [45,49], the boundary lubrication of the system should not be affected by the change from water vapor to liquid water [19] or from IPA vapor to liquid IPA. However, there is an important difference between the vapor experiments and the liquid-immersed experiments: when the Si-on-Si interface is fully immersed in water or IPA, capillary adhesion is absent since capillary menisci can only form when a gas phase is present. The reduction in friction upon immersion can therefore be translated into a capillary adhesive force: $F_c = (\mathrm{COF}_{\mathrm{vapor}}/\mathrm{COF}_{\mathrm{immersed}} - 1) \times F_{\mathrm{ex}}$, where $\mathrm{COF}_{\mathrm{vapor}}$ and $\mathrm{COF}_{\mathrm{immersed}}$ are the COF measured in vapor and liquid-immersed environments, respectively. Implicit in this calculation is the assumption that the frictional force is proportional to the normal force (Fig. S3 in the Supplemental Material [44]) experienced by the asperities [30], an assumption that was recently confirmed in a similar system
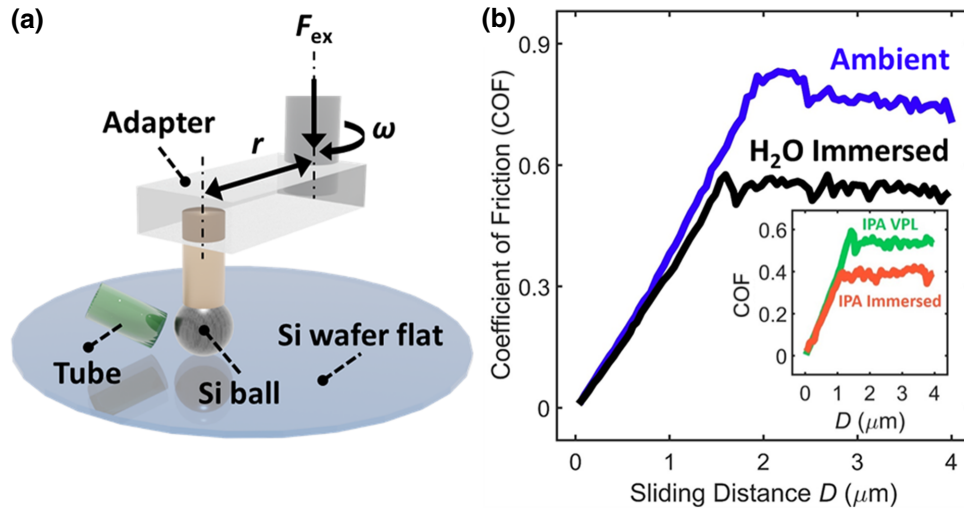
FIG. 3. Macroscopic siding experiment. (a) The Si ball-on-Si wafer friction measurements are performed using a customized rheometer that measures the normal force and torque exerted on a geometry to which the Si ball is clamped while it is slid at a constant externally applied normal force (F_{ex}) and angular velocity (ω). A plastic tube is mounted right next to the 3 mm ball to perform IPA vapor-phase lubrication friction experiments. The tube directs a gas flow of dry N_2 that is passed through a gas wash bottle filled with IPA towards the interface at a rate of 5 l/min (see Appendix E for more details). (b) The static and dynamic coefficient of friction (COF) are measured in ambient ($41 \pm 1\%$ RH) and water-immersed environments. The inset of (b) shows the COF measured in IPA vapor as described above and immersed in IPA. All measurements are performed at a normal force of 40 mN and a sliding velocity of 1 μm/s.

[31]. The capillary adhesion thus calculated for both water (41% RH) and IPA-rich vapor environments is 23 ± 5 and 8 ± 5 mN, respectively. We observe stronger capillary adhesion in the ambient environment than in the IPA environment, as in the AFM measurements. However, the capillary adhesion estimated from the sliding experiments (23 ± 5 mN) is significantly larger than that calculated for the interface under 40 mN externally applied load [2.8 mN, Fig. 1(d)]. Furthermore, we find that in the absence of capillary adhesion (immersed conditions), the COF for the IPA experiment is about 30% lower than that measured in water [Fig. 3(b)]. This reduction in COF may be attributed to the difference in boundary lubrication between water and IPA [40].

D. Capillary adhesion and wear

To understand the discrepancy between the calculated (2.8 mN) and experimentally estimated (23 ± 5 mN) water capillary adhesive force in more detail, we return to the contact calculations. Since the contact calculations are based on the topography of the Si ball measured by AFM before performing sliding experiments, the calculations may not represent the experimental interface accurately. AFM topography measurements performed on the Si ball after the sliding experiment reveal a circular wear scar. To estimate how much material was removed from the sphere, we calculated the volume of the spherical cap (Fig. S4 in the Supplemental Material [44]) corresponding

to the wear scar and found an average wear volume of $V_{avg} = 4.3 \pm 1.3 \times 10^9$ nm³ based on four independent sliding experiments. The average total sliding distance for the four experiments was 205 μm (D_{Tot}, Table SIII in the Supplemental Material [44]) and the normal force (F_{ex}) was 40 mN, leading to a specific wear rate (K) of the Si ball that is $K = V_{avg}/F_{ex}D_{Tot} = 5.2 \times 10^5$ μm³/Nm, which can be interpreted as mild wear.

We emphasize that most wear is expected to take place when sharp and high asperities on the Si ball are removed during the very first stroke, as demonstrated previously [33]. The cross-section height profiles of the Si ball surface taken after sliding indeed show that high asperities are removed from the Si ball [the red curve in Fig. 2(e)], resulting in a reduced root-mean-square (rms) roughness [R_q, calculated along the 1.5 μm profile in Fig. 2(f)] as low as 0.9 nm in the contacting regions, comparable to the roughness of the Si wafer counter surface. To mimic this dynamic material removal process, we analyze the AFM topography recorded before the sliding experiments as follows. First, we remove the sphere curvature from the data. Next, we cut the highest asperities off the topography [Fig. 2(a)] by setting all heights above a (variable) threshold value equal to that threshold value. Subsequently, we impose the Si wafer roughness on top of the cut (flattened) areas of the topography [Fig. 2(b)]. This last step is motivated by the observation [Figs. 2(d)–2(f)] that worn areas on the Si ball display a roughness akin to that of the counter
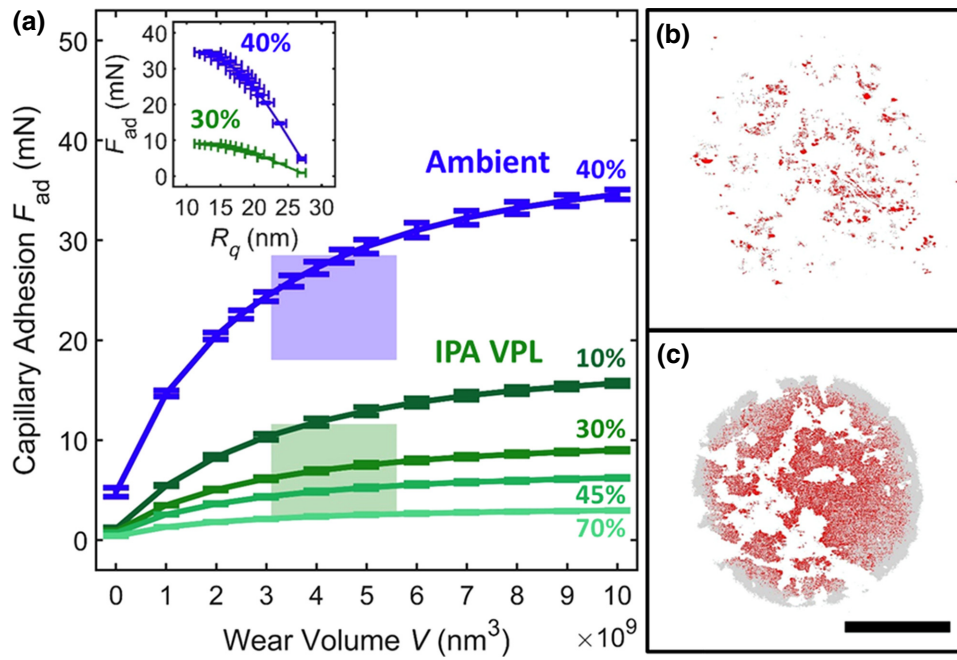
FIG. 4. Si ball-on-Si wafer capillary adhesion calculations and experiments. (a) Calculated capillary adhesion (F_{ad}) at 40 mN external load in ambient (40% relative humidity, blue line) and 10%–70% partial pressure of IPA vapor (green lines) environments as a function of wear volume (V). The adhesive forces in (a) were calculated based on the topographies of four independent Si balls; we report the average and the standard deviation of the results. The experimental estimates of the capillary adhesion and wear volume are reflected by the blue (ambient) and green (IPA) shaded squares. The capillary adhesion is plotted against the rms roughness (R_q) of the artificially worn Si ball in the inset of (a). The BEM contact calculations of solid–solid contacts (red) and capillary-wetted areas (grey, $W = 4$ nm) are shown for the pristine ($V = 0$ nm^3) Si ball (b) and the artificially worn ($V = 4 \times 10^9$ nm^3) Si ball (c). Scale bar 10 μm.

surface, the Si wafer. Once the topography has thus been artificially worn, we impose the sphere curvature again and run BEM calculations in which the artificially worn sphere is pressed onto a Si wafer. To calculate the artificial wear volume, we subtract the original topography from the worn topography [Figs. 2(a) and 2(b)].

We calculated the capillary adhesive force at the Si ball-on-Si wafer interface that is externally loaded with a force of 40 mN as a function of wear volume [Fig. 4(a)]. As the roughness of the sphere decreases due to increasing wear, an increase in capillary adhesion results [Fig. 4(a) inset]; worn topographies experience stronger adhesion. The reason for this is that high asperities on the ball surface initially prevent intimate contact between the two surfaces. As such asperities are removed, water bridges can form across more regions of the interface and therefore generate more capillary adhesion [37]. The model predicts that the adhesive force increases from 2.8 mN for the pristine surface to 28 mN for the Si ball surface from which $V_{avg} = 4.3 \times 10^9$ nm^3 of material was worn, in agreement with the experiments based on which an adhesive force of 23 ± 5 mN was found. This result is also in line with the analytical capillary adhesion model proposed by Persson [53] in which the capillary adhesion increases strongly

when the rms roughness of the interface approaches the range of the adhesion.

In addition to the water adhesion calculations, we performed contact calculations relating to the IPA vapor environment. However, because the precise composition of the gas surrounding the interface is unknown, we used literature values for W and $P_{Laplace}$ that correspond to an IPA partial pressure (P/P_{sat}) range of 10%–70%. According to our model the capillary adhesion increases with decreasing IPA partial pressure; the effect of increasing Laplace pressure with decreasing IPA partial pressure outweighs the decrease in the wetted area with decreasing partial pressure (decreasing W). The IPA capillary adhesion calculations as a function of wear show good agreement with the experimental estimates of the adhesive force and support the interpretation of our experiments and our model. The relative impact of capillary adhesion is greatly enhanced by wear, but can be minimized by replacing water in the environment with IPA. Furthermore, in the absence of capillary adhesion, Si-on-Si friction is lower in an IPA-immersed environment than in a water-immersed environment, suggesting that IPA is more effective as a boundary lubricant. The mechanism behind this boundary lubrication provided by IPA may lie in its ability to passivate bond-forming

species such as hydroxyl groups, thereby lowering the surface energy and friction [54,55]. Furthermore, IPA may suppress wear and slow down the wear-induced changes in adhesion [54].

III. CONCLUSION

We demonstrated that capillary adhesion dominates single-nanoasperity Si-on-Si pull-off force measurements. While strong capillary adhesion is present at loaded multiasperity interfaces, the adhesion disappears when the load is removed. Nonetheless, the capillary adhesive force at a loaded multiasperity interface significantly increases friction. Wear of the highest roughness peaks drastically reduces the average interfacial gap, thereby further increasing adhesion and friction. This interplay between capillary adhesion, wear-induced topography changes, and friction was successfully captured by a boundary element model without adjustable parameters. One assumption in the model is that the capillary bridges are in equilibrium with the surrounding vapor. This assumption is known to break down at velocities above 100 μm/s [56], well above the sliding speeds (and pull-off speeds) investigated in this work. Capillary adhesion and wear can easily lead to failure of devices that involve silicon-based interfaces with nanoscale surface roughness such as MEMS and NEMS. The latter is known to occur through nanoscale wear processes. [41] Our model can be used to predict the friction behavior and failure of stiff hydrophilic interfaces in general [31]. Furthermore, we showed that replacement of water with IPA strongly reduces capillary adhesion and improves boundary lubrication. These insights pave the way for better control over friction and wear in demanding high-tech applications such as the positioning systems used in the semiconductor manufacturing industry.

ACKNOWLEDGMENTS

APPENDIX A: AFM-BASED SINGLE-ASPERITY ADHESION MEASUREMENTS

The single-asperity pull-off experiments were performed by using AFM (Dimension Icon, Bruker) in four environmental conditions: IPA or water vapors and IPA or water liquids. The various gas environments are established by flowing water-saturated N_2 or IPA-saturated N_2 into the semiopen fluid AFM cell (Bruker) at a fixed flow rate of 0.5 l/min while the lab humidity was maintained at 50% RH. We introduced an equilibration time of 30 min after each change in environment to ensure a steady-state gas mixture in the liquid cell. The normal displacement of the AFM probe is imposed by the piezo tube that holds at the end of the AFM cantilever adjacent to the tip. Typical force-displacement (*F-D*) curves [Figs. 1(a) and 1(b)] were recorded by approaching the Si wafer with the AFM tip and subsequently retracting the tip, both at a speed of 5 nm/s, while measuring the normal force exerted at the interface. In the vapor environments we used a Si AFM tip (RTESPA-300, Bruker), and in the liquid-immersed measurements (which lack capillary effects) we used a Si_3N_4 tip (ScanAsyst-Fluid).

APPENDIX B: MACROSCOPIC ADHESION MEASUREMENT

The macroscopic pull-off experiments are carried out using a universal mechanical tester (UMT Tribolab, Bruker) in an ambient air environment ($53 \pm 1.4\%$ RH). A Si ball is mounted on the force sensor (DFM-0.5G, Bruker, 1.94×10^3 N/m normal stiffness). The force sensor measures 1 mN minimum force with 0.25 mN resolution. The Si ball is preloaded onto a Si wafer substrate at 40 mN, and retracted from the Si wafer with 2 μm/s pull-off speed. The native oxide layer of Si is expected to form on both Si ball and Si wafer surfaces.

APPENDIX C: SURFACE CHARACTERIZATION

The surface topography of the contacting bodies is measured by tapping mode AFM (Dimension Icon, Bruker) with Si tips (RTESPA-300, Bruker).

APPENDIX D: MULTIASPERITY CAPILLARY ADHESION CALCULATION

The calculation of capillary adhesion exerted at multiasperity interfaces consists of two parts: contact calculations based on the BEM [57] and calculations of the area wetted by the capillary liquid (A_{cap}) at the interfaces. First, the area of real contact at the Si ball-on-Si wafer interface is estimated by BEM contact calculations in which the elastoplastic equations that describe the deformed interface are solved. We employ the contact calculations by using the Tribology Simulator [58]. As input, the calculations make use of the measured AFM surface topography of the Si ball with about 1.7×10^3 nm^2 per pixel. The contact calculation was carried out at 40 mN elastic force ($F_{elastic}$) and the mechanical properties of the Si ball and the Si wafer are reported in Table SII in the Supplemental Material [44]. The result of contact calculation is shown in Figs. 4(b) and 4(c) where the solid–solid area of real contact is indicated in red. Second, we estimate the wetted area (A_{cap}) across the interface [gray area in Figs. 4(b) and 4(c)]

where capillary adhesion occurs as described in Sec. II in the main text. The capillary adhesion is caused by the pressure difference between gaseous and liquid environments as quantified by the Laplace pressure (P_{Laplace}) of the capillary meniscus. The capillary meniscus at the hydrophilic interface is characterized by a positive radius of curvature (r_1) in the in-plane direction and a negative radius (r_2) of curvature in the out-of-plane direction as illustrated in the inset of Fig. 1(b). Because $|r_1| \gg |r_2|$ the overall radius of curvature ($1/R = 1/r_1 + 1/r_2$) of the capillary meniscus can be approximated as $R \approx r_2$ such that the Laplace pressure is dominated by the negative radius of meniscus curvature. The P_{Laplace} estimated based on the Kelvin–Tolman equation is given by $P_{\text{Laplace}} = \gamma/(r_2 + \delta)$, where γ the bulk liquid surface tension (see Supplemental Material I [44]), $r_2 = -d_c/2$ and δ the Tolman length ($\delta = 0.2$ nm at 40%–50% RH). [45] Thus, combining the above calculations, the capillary adhesion exerted at multiasperity interfaces (F_{ad}) is calculated as $F_{\text{ad}} = P_{\text{Laplace}} \times A_{\text{cap}}$.

APPENDIX E: MACROSCOPIC SLIDING EXPERIMENT

Ball-on-flat friction experiments are performed using a customized rheometer setup (DSR 301, Anton Paar) in four different environmental conditions: ambient air ($\sim$40% RH), IPA vapor, and liquid-water- and IPA-immersed environments [Fig. 3(a)]. The 3-mm-diameter Si ball ($R_q = 28.3$ nm over a $85 \times 85\ \mu$m scan area with 430.6 nm^2 pixel size) was slid against Si flat ($R_q = 0.9$ nm over a $5 \times 5\ \mu$m scan area [41]) at a constant angular velocity ($\omega = 8.3 \times 10^{-5}$ rad/s) that can be converted into a constant sliding speed by multiplication with the fixed rotation radius ($r = 12.98$ mm): $V = \omega r = 1\ \mu$m/s. The applied normal force was manually adjusted to approximately 40 mN. At 40 mN normal force, the Hertzian contact pressure (P_{Hertz}) is determined to be approximately 250 MPa. In order to minimize wear-induced changes in friction, the measurements were performed as separate strokes: each stroke on a previously untouched piece of Si wafer to prevent the interaction between the sliding contact and wear debris [41]. The stroke length for each Si ball in the experiments is listed in Table SIII in the Supplemental Material [44] and was minimized to avoid wear of the balls. The IPA gas flows were supplied at a constant flow rate of 5 l/min through a plastic tube with an inner diameter of 4 mm. The tube outlet was directed at the contact and situated at a distance of up to 1 cm from the contact. Dry N$_2$ saturated with IPA vapor was generated by passing dry N$_2$ through a liquid IPA bubbler. In all experiments the flow was turned on before creating contacts. Each set of sliding experiments was repeated at least three times under the same environmental conditions.

[1] E. Soylemez and M. P. de Boer, Capillary-induced crack healing between surfaces of nanoscale roughness, Langmuir **30**, 11625 (2014).

[2] M. D. Butler and D. Vella, Liquid bridge splitting enhances normal capillary adhesion and resistance to shear on rough surfaces, J. Colloid Interface Sci. **607**, 514 (2022).

[3] L. Xue, A. Kovalev, A. Eichler-Volf, M. Steinhart, and S. N. Gorb, Humidity-enhanced wet adhesion on insect-inspired fibrillar adhesive pads, Nat. Commun. **6**, 6621 (2015).

[4] S. Gernay, W. Federle, P. Lambert, and T. Gilet, Elasto-Capillarity in insect fibrillar adhesion, J. R. Soc. Interface **13**, 20160371 (2016).

[5] M. Pakpour, M. Habibi, P. Møller, and D. Bonn, How to construct the perfect sandcastle, Sci. Rep. **2**, 549 (2012).

[6] J. A. Williams and H. R. Le, Tribology and MEMS, J. Phys. D: Appl. Phys. **39**, R201 (2006).

[7] S. H. Kim, D. B. Asay, and M. T. Dugger, Nanotribology and MEMS, Nano Today **2**, 22 (2007).

[8] A. I. Vakis, *et al.*, Modeling and simulation in tribology across scales: An overview, Tribol. Int. **125**, 169 (2018).

[9] O. Hod, E. Meyer, Q. Zheng, and M. Urbakh, Structural superlubricity and ultralow friction across the length scales, Nature **563**, 485 (2018).

[10] O. Y. Loh and H. D. Espinosa, Nanoelectromechanical contact switches, Nat. Nanotechnol. **7**, 283 (2012).

[11] P. F. Ferrari, S. Kim, and A. M. van der Zande, Dissipation from interlayer friction in graphene nanoelectromechanical resonators, Nano Lett. **21**, 8058 (2021).

[12] A. Ghanbarzadeh-Dagheyan, N. Jalili, and M. T. Ahmadian, A holistic survey on mechatronic systems in micro/nano scale with challenges and applications, J. Micro-Bio Rob. **17**, 1 (2021).

[13] Y. Tian, Z. Huo, F. Wang, C. Liang, B. Shi, and D. Zhang, A novel friction-actuated 2-DOF high precision positioning stage with hybrid decoupling structure, Mech. Mach. Theory **167**, 104511 (2022).

[14] D. Kang, X. Dong, H. Kim, P. Park, and C. E. Okwudire, Friction isolated rotary system for high-precision roll-to-roll manufacturing, Precision Eng. **68**, 358 (2021).

[15] Y.-H. Sun, T. Chen, C. Qiong Wu, and C. Shafai, Comparison of four friction models: Feature prediction, J. Comput. Nonlinear Dynamics **11**, 1 (2016).

[16] S. Thiery, M. Kunze, A. Karimi, A. Curnier, and R. Longchamp, in *2006 American Control Conference*, Vol. 2006 (IEEE, 2006), 5 pp.

[17] K. Hasz, Z. Ye, A. Martini, and R. W. Carpick, Experiments and simulations of the humidity dependence of friction between nanoasperities and graphite: The role of interfacial contact quality, Phys. Rev. Mater. **2**, 126001 (2018).

[18] C. Greiner, J. R. Felts, Z. Dai, W. P. King, and R. W. Carpick, Controlling nanoscale friction through the competition between capillary adsorption and thermally activated sliding, ACS Nano **6**, 4305 (2012).

[19] L. Chen, C. Xiao, B. Yu, S. H. Kim, and L. Qian, What governs friction of silicon oxide in humid environment: Contact area between solids, water meniscus around the contact, or water layer structure?, Langmuir **33**, 9673 (2017).

[20] M. Bartošík, L. Kormoš, L. Flajšman, R. Kalousek, J. Mach, Z. Lišková, D. Nezval, V. Švarc, T. Šamořil, and T. Šikola, Nanometer-sized water bridge and pull-off force

in AFM at different relative humidities: Reproducibility measurement and model based on surface tension change, J. Phys. Chem. B **121**, 610 (2017).

[21] E. Riedo, F. Lévy, and H. Brune, Kinetics of Capillary Condensation in Nanoscopic Sliding Friction, Phys. Rev. Lett. **88**, 185505 (2002).

[22] M. Lee, B. Kim, J. Kim, and W. Jhe, Noncontact friction via capillary shear interaction at nanoscale, Nat. Commun. **6**, 7359 (2015).

[23] T.-D. Li, H.-C. Chiu, D. Ortiz-Young, and E. Riedo, Nanorheology by atomic force microscopy, Rev. Sci. Instrum. **85**, 123707 (2014).

[24] D. Ortiz-Young, H.-C. Chiu, S. Kim, K. Voïtchovsky, and E. Riedo, The interplay between apparent viscosity and wettability in nanoconfined water, Nat. Commun. **4**, 2482 (2013).

[25] C. Xiao, P. Shi, W. Yan, L. Chen, L. Qian, and S. H. Kim, Thickness and structure of adsorbed water layer and effects on adhesion and friction at nanoasperity contact, Colloids Interfaces **3**, 55 (2019).

[26] K. B. Jinesh and J. W. M. Frenken, Capillary Condensation in Atomic Scale Friction: How Water Acts Like a Glue, Phys. Rev. Lett. **96**, 166103 (2006).

[27] M. R. Uhlig and R. Garcia, In situ atomic-scale imaging of interfacial water under 3D nanoscale confinement, Nano Lett. **21**, 5593 (2021).

[28] L. Pastewka and M. O. Robbins, Contact between rough surfaces and a criterion for macroscopic adhesion, Proc. Natl. Acad. Sci. U. S. A. **111**, 3298 (2014).

[29] X. He, Z. Liu, L. B. Ripley, V. L. Swensen, I. J. Griffin-Wiesner, B. R. Gulner, G. R. McAndrews, R. J. Wieser, B. P. Borovsky, Q. J. Wang, and S. H. Kim, Empirical relationship between interfacial shear stress and contact pressure in micro- and macro-scale friction, Tribol. Int. **155**, 106780 (2021).

[30] A. Berman, C. Drummond, and J. Israelachvili, Amontons' law at the molecular level, Tribol. Lett. **4**, 95 (1998).

[31] F.-C. Hsia, S. Franklin, P. Audebert, A. M. Brouwer, D. Bonn, and B. Weber, Rougher is more slippery: How adhesive friction decreases with increasing surface roughness due to the suppression of capillary adhesion, Phys. Rev. Res. **3**, 043204 (2021).

[32] H. Sakuma, K. Kawai, I. Katayama, and S. Suehara, What is the origin of macroscopic friction?, Sci. Adv. **4**, eaav2268 (2018).

[33] F.-C. Hsia, F. M. Elam, D. Bonn, B. Weber, and S. E. Franklin, Tracing single asperity wear in relation to macroscale friction during running-In, Tribol. Int. **162**, 107108 (2021).

[34] M. Bazrafshan, M. B. de Rooij, and D. J. Schipper, Adhesive force model at a rough interface in the presence of thin water films: The role of relative humidity, Int. J. Mech. Sci. **140**, 471 (2018).

[35] J. Wang, J. Qian, and H. Gao, Effects of capillary condensation in adhesion between rough surfaces, Langmuir **25**, 11727 (2009).

[36] M. Sedighi, V. B. Svetovoy, and G. Palasantzas, Capillary-force measurement on SiC surfaces, Phys. Rev. E **93**, 062803 (2016).

[37] A. Tiwari, J. Wang, and B. N. J. Persson, Adhesion paradox: Why adhesion is usually not observed for macroscopic solids, Phys. Rev. E **102**, 042803 (2020).

[38] L. A. Thimons, A. Gujrati, A. Sanner, L. Pastewka, and T. D. B. Jacobs, Hard-material adhesion: Which scales of roughness matter?, Exp. Mech. **61**, 1109 (2021).

[39] S. Pham-Ba and J.-F. Molinari, Creation and evolution of roughness on silica under unlubricated wear, Wear **472–473**, 203648 (2021).

[40] D. B. Asay, E. Hsiao, and S. H. Kim, Effects of adsorbate coverage and capillary on nano-asperity friction in atmosphere containing organic vapor, J. Appl. Phys. **110**, 064326 (2011).

[41] F.-C. Hsia, F. M. Elam, D. Bonn, B. Weber, and S. E. Franklin, Wear particle dynamics drive the difference between repeated and non-repeated reciprocated sliding, Tribol. Int. **142**, 105983 (2020).

[42] T. Cramer, F. Zerbetto, and R. García, Molecular mechanism of water bridge buildup: Field-induced formation of nanoscale menisci, Langmuir **24**, 6116 (2008).

[43] S. Cheng and M. O. Robbins, Nanocapillary adhesion between parallel plates, Langmuir **32**, 7788 (2016).

[44] See Supplemental Material at http://link.aps.org/supplemental/10.1103/PhysRevApplied.17.034034 for more details of the adhesion calculation and experimental methods and results, which includes Refs. [59,60].

[45] S. Kim, D. Kim, J. Kim, S. An, and W. Jhe, Direct Evidence for Curvature-Dependent Surface Tension in Capillary Condensation: Kelvin Equation at Molecular Scale, Phys. Rev. X **8**, 041046 (2018).

[46] D. B. Asay and S. H. Kim, Evolution of the adsorbed water layer structure on silicon oxide at room temperature, J. Phys. Chem. B **109**, 16760 (2005).

[47] A. v. Pinon, M. Wierez-Kien, A. D. Craciun, N. Beyer, J. L. Gallani, and M. v. Rastei, Thermal effects on van Der Waals adhesive forces, Phys. Rev. B **93**, 035424 (2016).

[48] E. Soylemez and M. P. de Boer, Crack healing between rough polycrystalline silicon hydrophilic surfaces in N-pentanol and water vapors, Tribol. Lett. **59**, 5 (2015).

[49] D. Kim, J. Kim, J. Hwang, D. Shin, S. An, and W. Jhe, Direct measurement of curvature-dependent surface tension of an alcohol nanomeniscus, Nanoscale **13**, 6991 (2021).

[50] C. M. Mate and R. W. Carpick, *Tribology on the Small Scale* (Oxford Graduate Texts, Oxford, 2019), 2nd ed.

[51] S. Kelly, C. Torres-Verdín, and M. T. Balhoff, Anomalous liquid imbibition at the nanoscale: The critical role of interfacial deformations, Nanoscale **8**, 2751 (2016).

[52] D. B. Asay and S. H. Kim, Effects of adsorbed water layer structure on adhesion force of silicon oxide nanoasperity contact in humid ambient, J. Chem. Phys. **124**, 174712 (2006).

[53] B. N. J. Persson, Capillary adhesion between elastic solids with randomly rough surfaces, J. Phys.: Condens. Matter **20**, 315007 (2008).

[54] A. L. Barnette, D. B. Asay, D. Kim, B. D. Guyer, H. Lim, M. J. Janik, and S. H. Kim, Experimental and density functional theory study of the tribochemical wear behavior of SiO₂ in humid and alcohol vapor environments, Langmuir **25**, 13052 (2009).

[55] L. Chen, Y. J. Yang, H. T. He, S. H. Kim, and L. M. Qian, Effect of coadsorption of water and alcohol vapor on the nanowear of silicon, Wear **332–333**, 879 (2015).

[56] O. Noel, P.-E. Mazeran, and H. Nasrallah, Sliding Velocity Dependence of Adhesion in a Nanometer-Sized Contact, Phys. Rev. Lett. **108**, 015503 (2012).

[57] M. H. Müser, *et al.*, Meeting the contact-mechanics challenge, Tribol. Lett. **65**, 118 (2017).

[58] Publicly available at eww.tribology.org.

[59] D. Vorselen, E. S. Kooreman, G. J. L. Wuite, and W. H. Roos, Controlled tip wear on high roughness surfaces yields gradual broadening and rounding of cantilever tips, Sci. Rep. **6**, 36972 (2016).

[60] A. L. Barnette, D. B. Asay, M. J. Janik, and S. H. Kim, Adsorption isotherm and orientation of alcohols on hydrophilic SiO₂ under ambient conditions, J. Phys. Chem. C **113**, 10632 (2009).